APPLIED PHYSICS

Current-induced magnetization switching using an electrically insulating spin-torque generator

Hongyu An,[1] Takeo Ohno,[2,3] Yusuke Kanno,[1] Yuito Kageyama,[1] Yasuaki Monnai,[1] Hideyuki Maki,[1,3] Ji Shi,[4] Kazuya Ando[1,3]*

Copyright © 2018 The Authors, some rights reserved; exclusive licensee American Association for the Advancement of Science. No claim to original U.S. Government Works. Distributed under a Creative Commons Attribution NonCommercial License 4.0 (CC BY-NC).

Current-induced magnetization switching through spin-orbit torques is the fundamental building block of spin-orbitronics, which promises high-performance, low-power memory and logic devices. The spin-orbit torques generally arise from spin-orbit coupling of heavy metals. However, even in a heterostructure where a metallic magnet is sandwiched by two different insulators, a nonzero spin-orbit torque is expected because of the broken inversion symmetry; an electrical insulator can be a source of the spin-orbit torques. We demonstrate current-induced magnetization switching using an insulator. We show that oxygen incorporation into the most widely used spintronic material, Pt, turns the heavy metal into an electrically insulating generator of the spin-orbit torques, which enables the electrical switching of perpendicular magnetization in a ferrimagnet sandwiched by insulating oxides. We also show that the spin-orbit torques generated from the Pt oxide can be controlled electrically through voltage-driven oxygen migration. These findings open a route toward energy-efficient, voltage-programmable spin-orbit devices based on insulating metal oxides.

INTRODUCTION

An emerging direction in spintronics aims at discovering novel phenomena and functionalities originating from the spin-orbit coupling (SOC) in solid-state devices (*1*–*4*). Of particular recent scientific and technological interests are current-induced spin-orbit torques that are responsible for the manipulation of magnetization in ultrathin ferromagnetic metals (FMs) (*5*–*15*). The current-induced magnetization switching through the spin-orbit torques is generally observed in heterostructures with broken inversion symmetry, such as an ultrathin FM sandwiched between an oxide and a heavy metal (HM): oxide/FM/HM structures. In the heterostructure, the spin-orbit torques have two components with different symmetries: damping-like and field-like spin-orbit torques (*8*, *12*). Recent experimental and theoretical progress has revealed that the damping-like and field-like spin-orbit torques are generated by both the bulk and interface SOC (*16*, *17*).

The development of energy-efficient spin-orbit devices can be realized using an electrically insulating spin-torque generator, which is free from the energy dissipation in the bulk. So far, topological insulators with metallic surface states are the only known bulk insulating spin-torque source. However, it is natural to expect that an ordinary insulator can also be a source of the spin-orbit torques; nonzero spin-torque generation is expected in a heterostructure where a metallic magnet is sandwiched by two different ordinary insulators, because the spin-orbit torques due to the interface SOC originate from the broken symmetry of the heterostructure. However, despite the recent vital progress in spin-orbitronics, the realization of magnetization manipulation using an insulating spin-torque generator remains elusive.

Here, we demonstrate current-induced magnetization switching using an ordinary insulator. We show that the widely used HM, Pt, becomes an electrically insulating generator of the spin-orbit torques after oxidation, enabling spin-torque magnetization switching in a heterostructure where a perpendicularly magnetized ferrimagnetic metal is sandwiched by two insulating oxides: MgO and oxidized Pt. We found that even in the absence of any conducting HM, the Pt oxide, attached to a metallic magnet, generates a robust damping-like spin-orbit torque purely through the interface SOC, which counters the conventional understandings of the spin-orbit torques, where the origin of the damping-like torque is primarily attributed to the bulk SOC. We also show that the relative strength of the damping-like and field-like torques changes systematically depending on the oxidation level of the Pt layer. This allows electrical tuning of the spin-orbit torques in a nonvolatile manner through voltage-driven O^{2-} migration near the FM/Pt-oxide interface. These results provide important information for revealing the underlying physics behind the current-induced spin-orbit torques, opening a way for insulator-based spin-orbitronics.

RESULTS

Current-induced magnetization switching

The device for the current-induced magnetization switching using an electrically insulating spin-torque generator is a MgO (1.4 nm)/CoTb (4.2 nm)/Pt(O) (8 nm)/substrate trilayer, capped with a Pt (1.7 nm) film, where the numbers in parentheses represent the thickness. Here, the atomic ratio of Tb in CoTb alloy was set as 0.25, and the thickness of the CoTb layer was set as 4.2 nm to obtain optimal perpendicular magnetic anisotropy on the Pt(O) layer (*18*, *19*). The films were patterned into a 20 μm × 80 μm Hall bar shape (Fig. 1A). The oxygen-incorporated Pt [Pt(O)] film was deposited on a thermally oxidized Si (SiO_2) substrate at room temperature by radio-frequency (rf) magnetron sputtering (for details, see Materials and Methods and fig. S1) (*20*). For the sputtering, argon and oxygen gases were introduced into the chamber, and the amount of oxygen gas in the reactive mixture, *Q*, was set as 16% for the current-induced magnetization switching experiment. A challenge in realizing the current-induced magnetization switching is the fabrication of an FM layer with perpendicular magnetic anisotropy on the Pt(O) film. We tried the commonly used Co and CoFeB as the FM layer. However, their magnetic anisotropy strongly depends on the interfacial conditions, which precludes obtaining perpendicular magnetic anisotropy on the Pt(O) film. Ni/Co multilayers

[1]Department of Applied Physics and Physico-Informatics, Keio University, Yokohama 223-8522, Japan. [2]World Premier International Research Center Initiative, Advanced Institute for Materials Research, Tohoku University, Sendai 980-8577, Japan. [3]PRESTO (Precursory Research for Embryonic Science and Technology), Japan Science and Technology Agency, Kawaguchi, Saitama 332-0012, Japan. [4]School of Materials and Chemical Technology, Tokyo Institute of Technology, Tokyo 152-8552, Japan.
*Corresponding author. Email: ando@appi.keio.ac.jp

Downloaded from http://advances.sciencemag.org/ on September 22, 2019

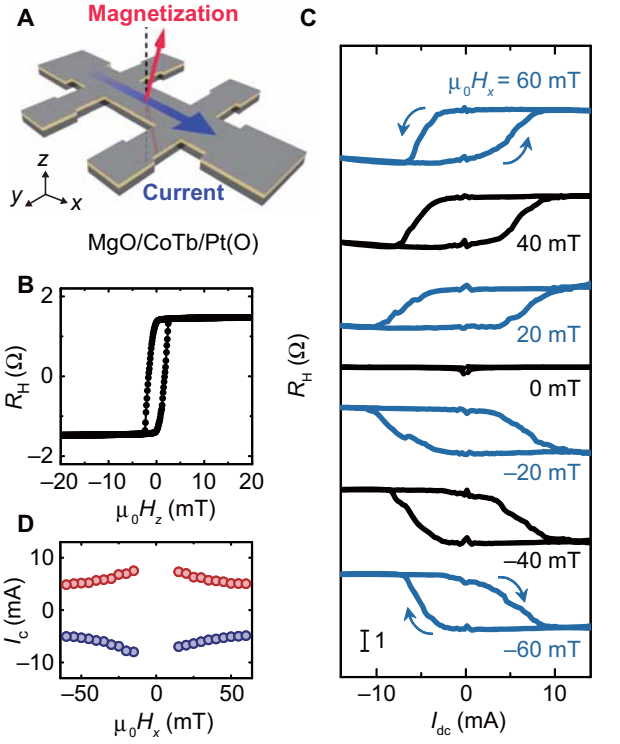

Fig. 1. Current-induced magnetization switching. (**A**) Schematic of the MgO/CoTb/Pt(O) heterostructure used for the AHE measurements. The charge current I_{dc} and external magnetic field were applied along the *x* axis for magnetization switching. (**B**) The anomalous Hall effect (AHE) resistance R_H measured by varying the perpendicular magnetic field $\mu_0 H_z$ for the MgO/CoTb/Pt(O) device. (**C**) Current-induced magnetization switching curves for the MgO/CoTb/Pt(O) heterostructure measured with different in-plane external magnetic fields $\mu_0 H_x$. (**D**) Switching phase diagram for the MgO/CoTb/Pt(O) heterostructure, where I_c is the switching current.

also cannot be used as the FM layer, because to obtain large perpendicular magnetic anisotropy of the multilayer, the strong face-centered cubic (111) orientation and a proper underlayer that acts as a template for the crystalline growth are necessary (*21*). Thus, we chose a transition metal–rare earth ferrimagnetic alloy, CoTb, with robust perpendicular magnetic anisotropy in the bulk as the FM layer for the current-induced magnetization switching (*18*, *19*, *22*). Figure 1B shows the AHE resistance R_H for the MgO/CoTb/Pt(O) film measured by sweeping a perpendicular magnetic field $\mu_0 H_z$. The nearly square magnetic hysteresis loop of R_H demonstrates good perpendicular magnetic anisotropy in the MgO/CoTb/Pt(O) film.

In the MgO/CoTb/Pt(O) trilayer, because of the broken inversion symmetry along the growth direction, a nonzero spin-orbit torque is expected when passing a charge current. Thus, we next measure R_H as a function of an in-plane dc current I_{dc}. For the measurement, we applied an in-plane magnetic field $\mu_0 H_x$ along the *x* axis to break the rotational symmetry of the spin-orbit torque. As shown in Fig. 1C, by applying a nonzero magnetic field $\mu_0 H_x$, the current switches the magnetization of the CoTb layer between up and down directions. By reversing the direction of the magnetic field, the polarity of the magnetization switching is also reversed. When $\mu_0 H_x = 0$, magnetization switching disappears. The corresponding switching phase diagram is shown in Fig. 1D. This result shows that the switching current increases by decreasing the in-plane external field $\mu_0 H_x$, which is consistent with the magnetization switching induced by the spin-orbit torque. We also note that the change of the AHE resistance due to the current-induced magnetization switching is comparable to the resistance change expected for the full switching of the magnetization shown in Fig. 1B. This result supports the idea that magnetization is fully reversed by the spin-orbit torque in the MgO/CoTb/Pt(O) heterostructure.

The above experimental result unambiguously demonstrates the current-induced magnetization switching in the heterostructure of ferrimagnetic CoTb sandwiched by two oxides: MgO and Pt(O). This result indicates that a nonzero spin-orbit torque is generated in the heterostructure, despite the fact that the applied charge current flows only in the ferrimagnetic CoTb layer; the current flow in the bulk of the Pt(O) layer can be neglected because of the much larger resistivity of Pt(O) (22,917 microhm · cm) than that of CoTb (74 microhm · cm). In the MgO/CoTb/Pt(O) trilayer, because the ferrimagnetic layer is sandwiched between the electrically insulating oxides, only the MgO/CoTb and CoTb/Pt(O) interfaces can be responsible for the spin-orbit torque generation. Previous studies have shown that, by the Rashba effect, a MgO/FM interface primarily generates a field-like torque (*23*, *24*), which cannot be responsible for the current-induced switching in the heterostructure; to switch the magnetization, a sizable damping-like torque is required (*7*). We have confirmed the existence of a damping-like effective field in the heterostructure by measuring the second harmonic of the AHE resistance (fig. S2). This result suggests that the CoTb/Pt(O) interface is responsible for the spin-torque generation.

Generation of spin-orbit torques from oxygen-incorporated Pt

To systematically study the generation of the spin-orbit torques at the FM/Pt(O) interface, we measure the spin-torque ferromagnetic resonance (ST-FMR) for $Ni_{81}Fe_{19}$/Pt(O) bilayers with *Q* in the 0 to 35% range. As shown in Fig. 2A, after the deposition of a Pt(O) film, a 6-nm-thick $Ni_{81}Fe_{19}$ layer was deposited on the Pt(O) layer, and a 4-nm-thick SiO_2 capping layer was used to protect the $Ni_{81}Fe_{19}$ layer from oxidation. The SiO_2/$Ni_{81}Fe_{19}$/Pt(O) films were patterned into rectangular strips (width, 10 μm; length, 150 μm) using the photolithography and lift-off techniques. For the ST-FMR measurement, an rf charge current was applied along the longitudinal direction, and an in-plane external magnetic field **H** was applied with an angle of 45° from the longitudinal direction of the device. In the device, the rf charge current generates the spin-orbit torques as well as an Oersted field, driving magnetization precession in the $Ni_{81}Fe_{19}$ layer. The magnetization precession results in an oscillation of the resistance due to the anisotropic magnetoresistance in the $Ni_{81}Fe_{19}$ layer, which can be measured through the mixing dc voltage V_{mix} by using a bias tee (*25*). The mixing voltage V_{mix} is expressed as (*25*, *26*)

$$V_{mix} = S\frac{W^2}{(\mu_0 H - \mu_0 H_{FMR})^2 + W^2} + A\frac{W(\mu_0 H - \mu_0 H_{FMR})}{(\mu_0 H - \mu_0 H_{FMR})^2 + W^2} \quad (1)$$

where *S*, *A*, *W*, and $\mu_0 H_{FMR}$ are the magnitude of the symmetric component, the magnitude of the antisymmetric component, the spectral width, and the FMR field, respectively. Here, the symmetric component is proportional to the damping-like effective field H_{DL}, and the antisymmetric component is due to the sum of the Oersted field H_{Oe} and the field-like effective field H_{FL} (*27*).

Figure 2B shows the ST-FMR spectra V_{mix} for the SiO_2/$Ni_{81}Fe_{19}$/Pt(O) devices with $Q = 0$ and 10% measured at a frequency range of

Downloaded from http://advances.sciencemag.org/ on September 22, 2019

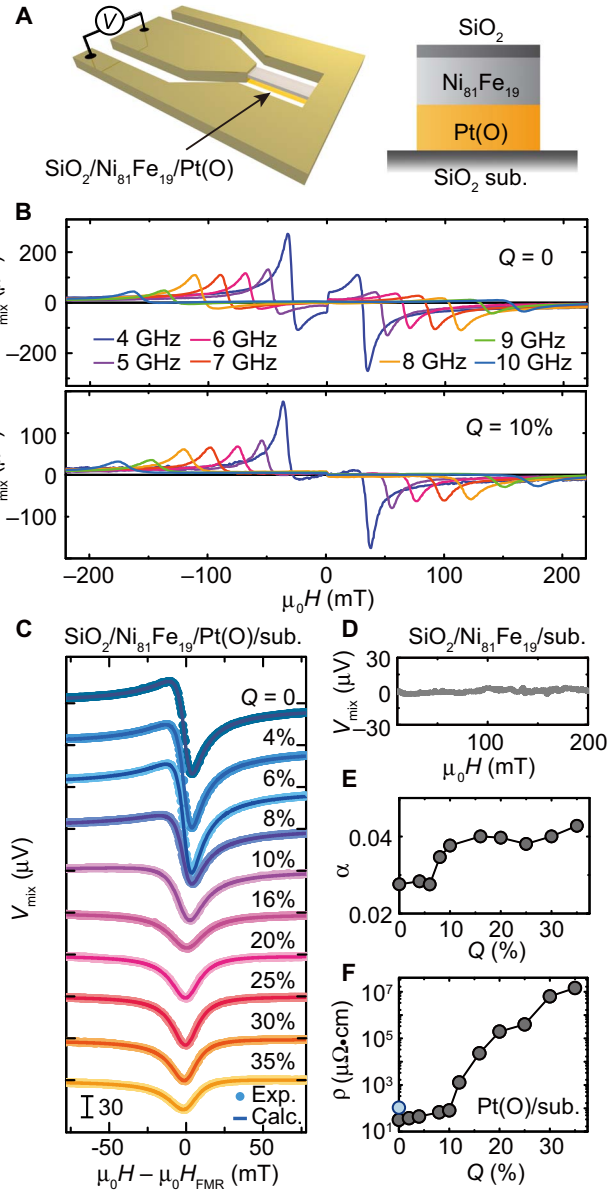

Fig. 2. ST-FMR measurements. (**A**) Schematic of the $SiO_2/Ni_{81}Fe_{19}/Pt(O)$ device for the ST-FMR measurements. (**B**) ST-FMR spectra for the $SiO_2/Ni_{81}Fe_{19}/Pt(O)$ devices by changing the rf current frequencies from 4 to 10 GHz, where $Q = 0$ and 10%. (**C**) ST-FMR spectra for the $SiO_2/Ni_{81}Fe_{19}/Pt(O)$ devices at 7 GHz by changing Q from 0 to 35%. The solid circles are the experimental data and the solid curves are the fitting result using Eq. 1. The rf power of 24.7 dBm was applied for all the measurements. (**D**) The ST-FMR spectrum for the $SiO_2/Ni_{81}Fe_{19}$ device at 7 GHz. (**E**) Q dependence of the magnetic damping constant α, obtained from the rf f dependence of the ST-FMR spectral width W using $W = (2\pi\alpha/\gamma)f + W_{ext}$, where γ is the gyromagnetic ratio and W_{ext} is the extrinsic contribution to the spectral width. (**F**) Q dependence of the electrical resistivity ρ of Pt(O) films. The blue solid circle shows the electrical resistivity of a $Ni_{81}Fe_{19}$ film.

4 to 10 GHz. As can be seen, by reversing the external magnetic field **H** direction, the sign of V_{mix} also changes correspondingly, as expected for the voltage generation induced by the ST-FMR. To systematically investigate the influence of the oxidation level in the Pt(O) films on the spin-torque generation, we have measured the ST-FMR for the $SiO_2/Ni_{81}Fe_{19}/Pt(O)$ films with different Q from 0 to 35% as shown in Fig. 2C. Notably, the spectral shape of V_{mix} changes markedly by increasing the amount of the oxygen gas flow Q; the ratio between symmetric and antisymmetric components, S/A, increases with increasing Q. This result shows that the spin-torque generation efficiency in the $SiO_2/Ni_{81}Fe_{19}/Pt(O)$ device is strongly affected by the oxidation level of the Pt(O) layer. We have confirmed that the voltage signal disappears in a $SiO_2/Ni_{81}Fe_{19}$ film fabricated on a SiO_2 substrate as shown in Fig. 2D, where the FMR field of the $Ni_{81}Fe_{19}$ layer is $\mu_0 H_{FMR} \sim 115$ mT. In the $SiO_2/Ni_{81}Fe_{19}$ film, a possible nonuniform current flow due to the electrode contacts can result in an antisymmetric voltage (*25*). The absence of the voltage signal in the $SiO_2/Ni_{81}Fe_{19}$ film supports the idea that the change in the spin-orbit torques generated from the Pt(O) layer is responsible for the change in the ST-FMR spectral shape in the $SiO_2/Ni_{81}Fe_{19}/Pt(O)$ films. We also note that previous studies have shown that the contribution to the symmetric component of the voltage signal from the spin pumping is negligible because of the large anisotropic magnetoresistance, which is the origin of the ST-FMR voltage, of $Ni_{81}Fe_{19}$ (*26*, *28*).

The observed change in the ST-FMR spectral shape is associated with the interface SOC in the $SiO_2/Ni_{81}Fe_{19}/Pt(O)$ films. In Fig. 2E, we show the magnetic damping constant α, determined from frequency dependence of the ST-FMR spectral width for the $SiO_2/Ni_{81}Fe_{19}/Pt(O)$ film with various Q. The magnetic damping α is enhanced by increasing the oxidation level of the Pt(O) layer, especially for $Q > 10\%$. In the $SiO_2/Ni_{81}Fe_{19}/Pt(O)$ film, the magnetic damping is dominated by the dissipation of the angular momentum induced by the spin pumping; the spin pumping emits a spin current from the $Ni_{81}Fe_{19}$ layer, and the absorption of the spin current outside the $Ni_{81}Fe_{19}$ layer deprives the magnetization of the angular momentum, giving rise to the additional magnetic damping (*29*). However, the magnetic damping enhanced by the oxygen incorporation in the $SiO_2/Ni_{81}Fe_{19}/Pt(O)$ film cannot be attributed to the spin absorption in the interior of the Pt(O) layer. When $Q > 10\%$, the electrical resistivity of the Pt(O) layer increases drastically with Q (Fig. 2F), and thus, the spin pumping into the bulk of the Pt(O) layer is strongly suppressed. With the spin absorption in the bulk of the Pt(O) layer ruled out as a mechanism behind the enhancement of the magnetic damping, the only possible mechanism that agrees with the experimental observation is the spin absorption at the $Ni_{81}Fe_{19}/Pt(O)$ interface. With strong interface SOC, the $Ni_{81}Fe_{19}/Pt(O)$ interface can be an efficient spin absorber because of the fast spin relaxation due to the spin-momentum coupling of the Rashba state and/or the efficient spin-flip scattering due to the SOC at the interface. Thus, the enhancement of the magnetic damping, as well as the change in the ST-FMR spectral shape, suggests that the strength of the SOC at the $Ni_{81}Fe_{19}/Pt(O)$ interface is enhanced by increasing the oxidation level of the Pt(O) layer.

To quantitatively investigate the influence of the oxidation level of the Pt(O) layer on the generation efficiency of the spin-orbit torques, we first determine the damping-like ξ_{DL} and field-like ξ_{FL} spin-torque efficiencies for the moderately oxidized Pt(O) films ($Q \leq 10$ %) by measuring the $Ni_{81}Fe_{19}$ layer thickness d_F dependence of the ST-FMR spectra. By increasing Q from 0 to 10%, the electrical resistivity of the Pt(O) films only increases from 32 to 81 microhm·cm as shown in Fig. 2F, which is still smaller than that of the $Ni_{81}Fe_{19}$ film (106 microhm·cm; see the blue solid circle in Fig. 2F). Therefore, the Oersted field created by the charge current flowing in the Pt(O) layer cannot be neglected in the $SiO_2/Ni_{81}Fe_{19}/Pt(O)$ film. In the presence of the Oersted field, the FMR spin-torque generation efficiency obtained from the resonance line shape

Downloaded from http://advances.sciencemag.org/ on September 22, 2019

$$\xi_{FMR} = \frac{S}{A}\frac{e\mu_0 M_s d_F d_N}{\hbar}\sqrt{1+\frac{\mu_0 M_s}{\mu_0 H_{FMR}}} \quad (2)$$

is related to the damping-like ξ_{DL} and field-like ξ_{FL} spin-torque efficiencies, under the assumption that $\xi_{DL(FL)}$ does not have a strong dependence on d_F in the range examined, as (*27*)

$$\frac{1}{\xi_{FMR}} = \frac{1}{\xi_{DL}}\left(1+\frac{\hbar}{e}\frac{\xi_{FL}}{\mu_0 M_s d_F d_N}\right) \quad (3)$$

where $\xi_{DL(FL)} = \mu_0 M_s d_F H_{DL(FL)}(2e/\hbar)/j_c^{Pt(O)}$. Here, d_F and d_N are the thicknesses of the $Ni_{81}Fe_{19}$ layer and Pt(O) layer, respectively. $j_c^{Pt(O)}$ is the charge current density in the Pt(O) layer and $\mu_0 M_s$ is the saturation magnetization. Figure 3 (A and B) shows the ST-FMR spectra for the $SiO_2/Ni_{81}Fe_{19}$/Pt(O) films with different d_F values ranging from 4 to 8 nm for Q = 0 and 10%. The ratio between symmetric and antisymmetric components S/A in both spectra increases by decreasing d_F. From the $1/d_F$ dependence of $1/\xi_{FMR}$ shown in Fig. 3C with Eq. 3, ξ_{DL} and ξ_{FL} are determined as shown in Fig. 4A. As shown, both ξ_{DL} and ξ_{FL} increase with Q; by increasing Q from 0 to 10%, ξ_{DL} increases from 0.044 to 0.059 and ξ_{FL} increases from − 0.0042 to − 0.017. The minus sign of ξ_{FL} indicates that the field-like effective field is opposite to the Oersted field. In Fig. 4B, ξ_{DL} and ξ_{FL} are replotted as a function of the electrical resistivity ρ of the Pt(O) layer. Here, in a system where the damping-like torque is purely generated by the bulk spin Hall effect, the damping-like spin-torque efficiency ξ_{DL} is equivalent to the effective spin Hall angle θ_{SHE} (*27*). Because θ_{SHE} is known to scale with the electrical resistivity ρ (*30*), the nonmonotonic change of ξ_{DL} with ρ shown in Fig. 4B suggests that the bulk spin Hall effect is not the only source of the observed spin-orbit torques in the $SiO_2/Ni_{81}Fe_{19}$/Pt(O) films with $Q \leq 10\%$. We also found that the relative magnitude of the field-like torque to the damping-like torque, $\xi_{FL}/\xi_{DL} = H_{FL}/H_{DL}$, increases with Q and ρ as shown in Fig. 4 (C and D).

By further increasing the oxidation level of the Pt(O) layer, the charge and spin transport in the $SiO_2/Ni_{81}Fe_{19}$/Pt(O) film change drastically. For $Q \geq 16\%$, the electrical resistivity of the Pt(O) films is larger than 2.3×10^4 microhm ·cm, which is more than two orders of magnitude larger than the resistivity of the $Ni_{81}Fe_{19}$ layer (see also Fig. 2F). This indicates that the flow of the applied rf charge current in the Pt(O) layer can be neglected for $Q \geq 16\%$. Consequently, the Oersted field arising from the charge current in the Pt(O) layer is negligible in the $SiO_2/Ni_{81}Fe_{19}$/Pt(O) films. This is evidenced in the ST-FMR spectra measured for different Pt(O) layer thicknesses shown in Fig. 5A. As can be seen, the ST-FMR spectral shape is independent of the thickness d_N of the Pt(O) layer for Q = 20%. Because the antisymmetric component of V_{mix} due to the Oersted field $H_{Oe} = d_N j_c^{Pt(O)}/2$ is proportional to the thickness of the Pt(O) layer d_N, the spectral shape is independent of d_N only when the charge current density $j_c^{Pt(O)}$ in the Pt(O) layer is negligible. The negligible $j_c^{Pt(O)}$ in the Pt(O) layer for $Q \geq 16\%$ is also confirmed by a numerical calculation using CST microwave studio.

In the absence of the charge current in the interior of the Pt(O) layer, the spin-orbit torques due to the bulk spin Hall effect, as well as the torque due to the Oersted field, are negligible. Nevertheless, we

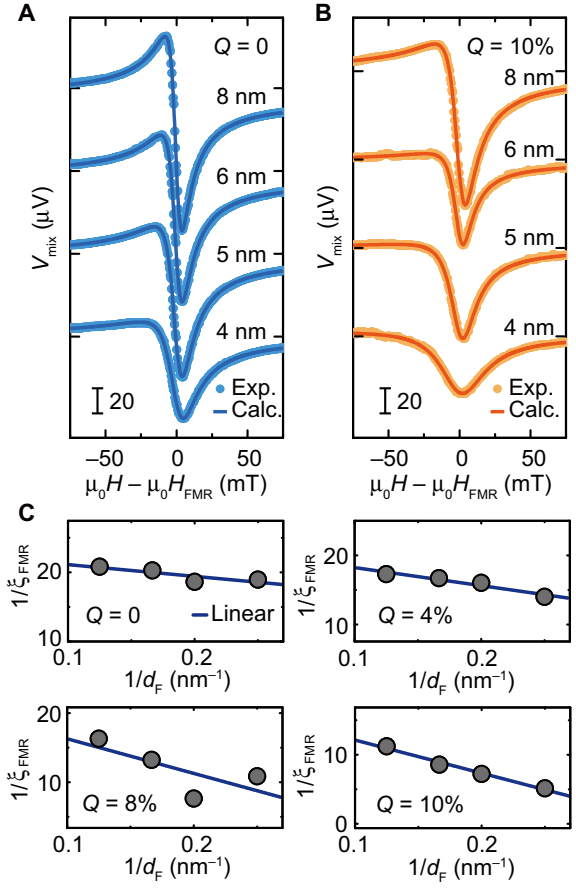

Fig. 3. Thickness dependence of ST-FMR. ST-FMR spectra for the $SiO_2/Ni_{81}Fe_{19}$/Pt(O) devices at 7 GHz when Q is (**A**) 0 and (**B**) 10%. The $Ni_{81}Fe_{19}$- layer thickness d_F was changed from 4 to 8 nm. (**C**) Inverse of the FMR spin-torque generation efficiency $1/\xi_{FMR}$ as a function of $1/d_F$ for Q = 0, 4, 8, and 10%. The solid circles are the experimental data and the solid lines are the linear fit to the data.

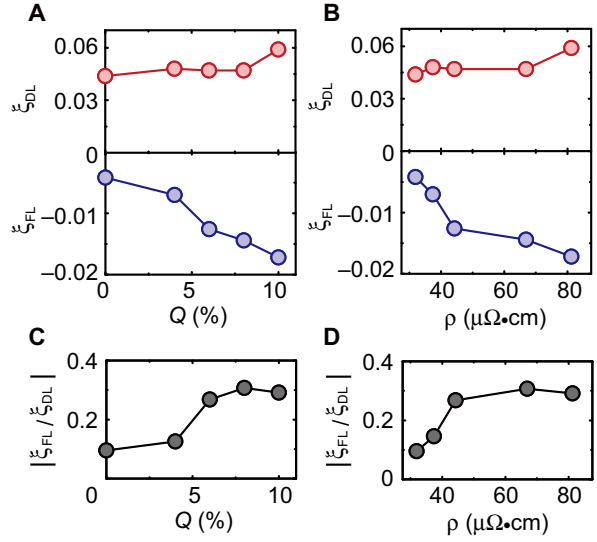

Fig. 4. Spin-torque generation efficiencies when *Q* is less than 10%. (**A**) Q dependence of the damping-like ξ_{DL} and field-like ξ_{FL} spin-torque generation efficiencies. (**B**) Pt(O) layer resistivity ρ dependence of ξ_{DL} and ξ_{FL}. (**C**) Q dependence of the ratio between ξ_{FL} and ξ_{DL}. (**D**) Pt(O) layer resistivity ρ dependence of the ratio between ξ_{FL} and ξ_{DL}.

Downloaded from http://advances.sciencemag.org/ on September 22, 2019

observed the clear ST-FMR signals for the $SiO_2/Ni_{81}Fe_{19}/Pt(O)$ devices with $Q \geq 16\%$ as shown in Fig. 2C. This result demonstrates that the current-induced FMR is driven by the spin-orbit toques purely generated at the $Ni_{81}Fe_{19}/Pt(O)$ interface. Figure 2C also shows that the sign of the antisymmetric component is reversed by increasing Q. This sign reversal originates from the disappearance of the Oersted field torque in the highly oxidized $Ni_{81}Fe_{19}/Pt(O)$ bilayers. In the bilayers with $Q > 16\%$, the field-like torque generates the antisymmetric voltage, whereas the Oersted field with the direction opposite to the field-like torque dominates the antisymmetric voltage in the $Ni_{81}Fe_{19}/Pt(O)$ bilayers with $Q < 10\%$. The change of the dominant contribution to the antisymmetric component, from the Oersted field to the field-like effective field, results in the sign reversal of the antisymmetric component of the ST-FMR signal by increasing Q. Here, the absence of the Oersted field in the device precludes the determination of the spin-torque efficiencies, ξ_{DL} and ξ_{FL}, with the self-calibrated Eqs. 2 and 3, used for $Q \leq 10\%$, where the strength of the spin-orbit torques from the charge current is measured relative to the torque from the Oersted field. The reason for this is that ξ_{DL} and ξ_{FL} are defined as the generation efficiency of the spin-orbit torques from the charge current density $j_c^{Pt(O)}$ flowing in the Pt(O) layer; ξ_{DL} and ξ_{FL} are undefined in the absence of $j_c^{Pt(O)}$. Under the negligible Oersted field, instead of the spin-torque efficiencies ξ_{DL} and ξ_{FL}, the relative magnitude of the field-like effective field H_{FL} to the damping-like effective field H_{DL} can be obtained directly from the ST-FMR spectral shape as

$$\frac{H_{FL}}{H_{DL}} = \frac{A}{S}\left(1 + \frac{\mu_0 M_s}{\mu_0 H_{FMR}}\right)^{-1/2} \quad (4)$$

In Fig. 5B, we show Q dependence of H_{FL}/H_{DL} obtained using Eq. 4. H_{FL}/H_{DL} is also plotted as a function of the Pt(O) layer resistivity ρ in Fig. 5C. Although these results show a significant increase of H_{FL}/H_{DL} with the oxidation of the Pt(O) layer, the damping-like torque is about an order of magnitude larger than the field-like torque in the trilayer, where the $Ni_{81}Fe_{19}$ layer is sandwiched by the two insulating oxides. This observation is quite consistent with the result in our current-induced magnetization switching experiment that the damping-like torque is responsible for the switching but contrary to the prediction of the spin-orbit torques generated by the interface Rashba effect; previous experimental and theoretical results suggest that the Rashba-Edelstein effect primarily generates the field-like torque (*16*, *17*). Our results therefore require a new source of the spin-orbit torques, other than the bulk spin Hall effect and interface Rashba-Edelstein effect, in the highly oxidized $SiO_2/Ni_{81}Fe_{19}/Pt(O)$ films.

A possible origin of the spin-orbit torques in the highly oxidized $SiO_2/Ni_{81}Fe_{19}/Pt(O)$ films is interfacial spin-dependent scattering (*31*, *32*). With strong interface SOC, the interfacial spin-orbit scattering creates spin currents that can flow away from the interface, which enter the ferromagnetic layer. This mechanism can exert torques on the magnetization through the spin-transfer mechanism, allowing the spin-orbit torques to have a strong damping-like component (*32*), which is consistent with our observation. Another possible mechanism is the intrinsic spin-orbit torque (*33*). In a two-dimensional (2D) Rashba system, a spin-orbit effective field induces spin rotation, which results in nonequilibrium out-of-plane spin polarization of carriers that are exchange-coupled to the in-plane magnetization. The out-of-plane spin density induces the damping-like torque on the magnetization (*33*). Thus, with the assumption that the Rashba SOC is present at the $Ni_{81}Fe_{19}/Pt(O)$ interface, the observed damping-like torque can be explained by the intrinsic mechanism in the highly oxidized $SiO_2/Ni_{81}Fe_{19}/Pt(O)$ films.

To characterize the generation efficiency of the damping-like and field-like torques for the $SiO_2/Ni_{81}Fe_{19}/Pt(O)$ device with $Q \geq 16\%$, we measured the ST-FMR by applying a dc charge current I_{dc}. In the $SiO_2/Ni_{81}Fe_{19}/Pt(O)$ device, the damping-like torque generated by the dc charge current I_{dc} effectively changes the magnetic damping α of the $Ni_{81}Fe_{19}$ layer or the FMR spectral width W, as shown in Fig. 5D. The damping modulation enables the determination of the conversion efficiency from the applied charge current I_{dc} to the damping-like effective field H_{DL}. Here, note that for $Q \geq 16\%$, the applied charge current flows only in the $Ni_{81}Fe_{19}$ layer, and thus the damping modulation allows one to determine the generation efficiency of the damping-like torque from the charge current density j_c^{Py} flowing in the $Ni_{81}Fe_{19}$ layer: $\bar{\xi}_{DL} = \mu_0 M_s d_F H_{DL}(2e/\hbar)/j_c^{Py}$, which is different from $\xi_{DL} = \mu_0 M_s d_F H_{DL}(2e/\hbar)/j_c^{Pt(O)}$ obtained for $Q \leq 10$ %.

We also note that the damping-like effective field H_{DL} for $Q \geq 16\%$ is generated by the charge current flowing at the $Ni_{81}Fe_{19}/Pt(O)$ interface. To characterize the spin-orbit torques generated by the 2D interface current j_c^I, we calculated the generation efficiency of the damping-like torque $\xi_{DL}^I = \mu_0 M_s d_F H_{DL}(2e/\hbar)/j_c^I$ as shown in Fig. 5E, where the 2D interface current is approximated as $j_c^I = t_I j_c^{Py}$ with an interface thickness

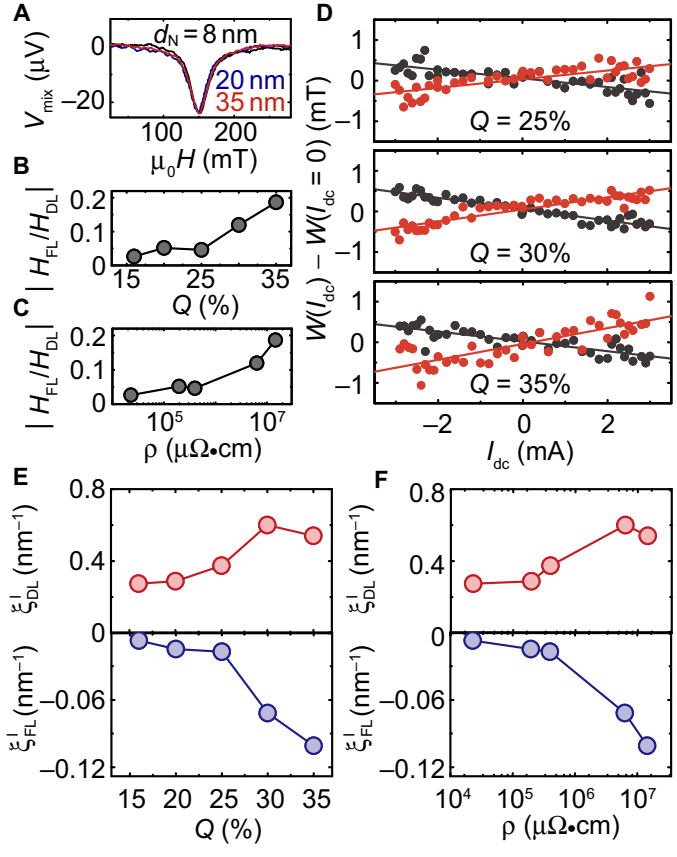

Fig. 5. Spin-torque generation efficiencies when *Q* is greater than 16%. (**A**) Pt(O) layer thickness d_N dependence of the ST-FMR spectra for the $SiO_2/Ni_{81}Fe_{19}/Pt(O)$ devices at 7 GHz with $Q = 20\%$. (**B**) Q dependence of the ratio between the damping-like H_{DL} and field-like H_{FL} effective fields. (**C**) Pt(O) layer resistivity ρ dependence of the ratio between H_{DL} and H_{FL}. (**D**) The change of the linewidth $W(I_{dc})$ of the ST-FMR spectrum as a function of the applied dc current I_{dc} for different Q. (**E**) Q dependence of ξ_{DL}^I and ξ_{FL}^I. (**F**) ρ dependence of ξ_{DL}^I and ξ_{FL}^I.

Downloaded from http://advances.sciencemag.org/ on September 22, 2019

of t_I = 0.5 nm (*34*, *35*). The obtained damping-like torque efficiency ξ^I_{DL} for the $SiO_2/Ni_{81}Fe_{19}/Pt(O)$ device is comparable to that for a topological insulator, where the spin-momentum locking of the surface state is responsible for the charge-spin conversion (*35*) and larger than that for a Bi/Ag interface with the giant Rashba effect (*34*).

This result demonstrates that the $Ni_{81}Fe_{19}/Pt(O)$ interface provides an efficient system to generate spin-orbit torques, enabling magnetization manipulation. The ξ^I_{DL} result also allows the determination of the generation efficiency, ξ^I_{FL}, of the field-like torque from j_c^I using $\xi^I_{FL}/\xi^I_{DL} = H_{FL}/H_{DL}$ with the measured values of H_{FL}/H_{DL} shown in Fig. 5 (B and C). As shown in Fig. 5 (E and F), the field-like torque efficiency ξ^I_{FL} increases markedly with the oxidation level of the Pt(O) layer, illustrating a crucial role of the oxidation of the Pt layer for the field-like torque generation.

Voltage control of spin-orbit torques

The above study unambiguously reveals the significant influence of the oxidation level of the $Ni_{81}Fe_{19}/Pt(O)$ bilayer on the spin-orbit torque generation and provides a probable approach to tune the spin-orbit torques through the voltage-driven O^{2-} migration near the $Ni_{81}Fe_{19}/Pt(O)$ interface. The voltage-driven O^{2-} migration has been well studied in a wide range of oxides so far (*36*–*42*). However, a crucial problem is that the oxygen concentration in the magnetron-sputtered Pt(O) films is too low to be used for O^{2-} migration even when we fabricated the Pt(O) film by using the oxygen flow Q of 100% during the deposition. To solve this problem, we fabricated a highly resistive PtO_x/PtO_y bilayer using the reactive sputtering and the oxygen plasma treatment as shown in Fig. 6A. The 7-nm-thick PtO_x layer was deposited by using the oxygen flow Q of 100% on the PtO_y layer, where the PtO_y layer was a magnetron-sputtered Pt layer oxidized by oxygen particle irradiation at the beginning (*43*, *44*); first, a 7.5-nm-thick Pt layer was deposited on a SiO_2 substrate, and then accelerated oxygen particles, extracted from the conventional oxygen plasma, passing through a biased electrode, were used to oxidize the Pt film. This oxygen plasma treatment leads to a formation of PtO_y with a depth of around 3.5 nm from the surface. The remaining nonoxidized Pt was used as the bottom electrode for the application of a gate voltage. The oxidized Pt layer created by the oxygen particle irradiation guarantees the sufficiently high oxygen concentration, and the PtO_x/PtO_y bilayer system provides an oxygen concentration gradient that favors O^{2-} migration (*39*–*41*). On the PtO_x/PtO_y bilayer, a 6-nm-thick $Ni_{81}Fe_{19}$ layer with a 4-nm-thick SiO_2 capping layer was deposited, which serves as both the FM layer for the ST-FMR measurement and the top electrode for the application of the gate voltage. For the $Ni_{81}Fe_{19}/PtO_x/PtO_y/Pt$ ($Ni_{81}Fe_{19}/Pt(O)/Pt$) device, we first applied the gate voltage between the top $Ni_{81}Fe_{19}$ and bottom Pt layers and then measured the ST-FMR after removing the gate voltage.

Figure 6B shows typical ST-FMR spectra measured after removing the gate voltage of ± 35 V from the $Ni_{81}Fe_{19}/Pt(O)/Pt$ device. The spectral shape of the ST-FMR changes by reversing the polarity of the gate voltage. Figure 6C summarizes the ratio between symmetric and antisymmetric components, S/A, obtained by fitting the ST-FMR spectra, which demonstrates reversible switching of the S/A ratio induced by the voltage application.

This reversible manipulation is best interpreted in terms of the switching of the spin-orbit torque generation due to internal O^{2-} or vacancy migration through nanoionic transport as illustrated in Fig. 6D. When the positive gate voltage (0 V → + 35 V → 0 V) was applied, the O^{2-} migrates toward the $Ni_{81}Fe_{19}/Pt(O)$ interface, leading to an increase of the S/A ratio

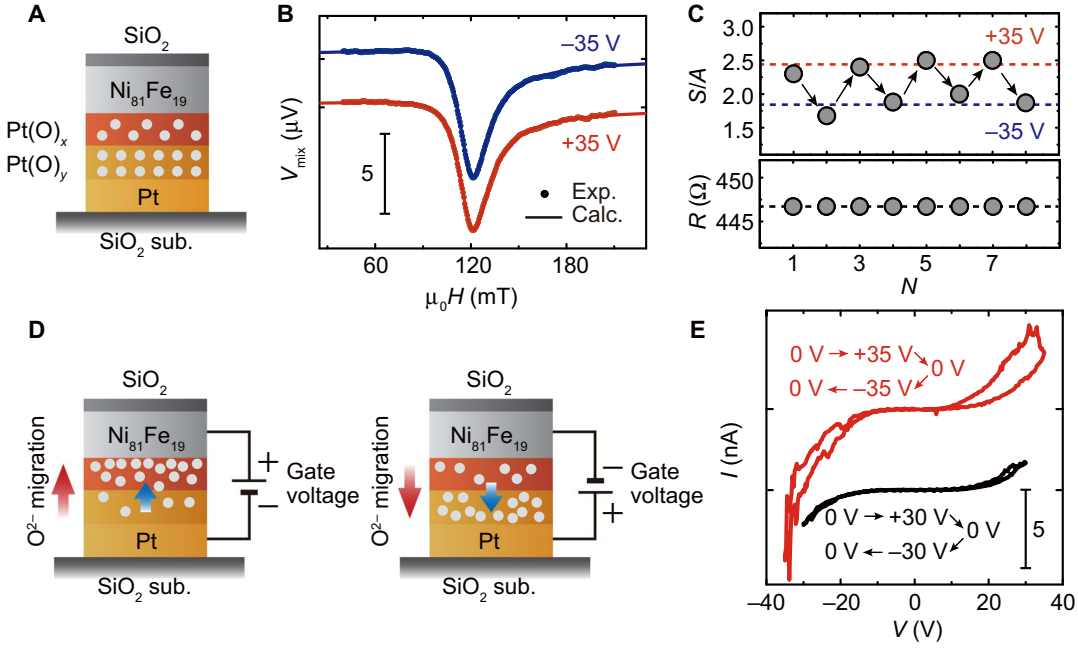

Fig. 6. Spin-torque generation controlled by O^{2-} migration. (**A**) Schematic of the heterostructure used for O^{2-} migration and ST-FMR measurement. The gray solid circles represent oxygen ions. (**B**) Typical ST-FMR spectra measured after removing the applied voltages of ± 35 V. The solid circles are the experimental data and the solid curves are the fitting result using Eq. 1. The offset of the curves in the vertical direction was shifted for comparison. (**C**) The magnitude of the S/A ratio obtained by fitting the corresponding ST-FMR spectra, where N represents the cycle index. The ST-FMR was measured for the $Ni_{81}Fe_{19}/Pt(O)/Pt$ device after the application of a gate voltage of + 35 V (N = 1, 3, 5, and 7) or −35 V (N = 2, 4, 6, and 8). The in-plane electrical resistance R of the $Ni_{81}Fe_{19}$ layer in the $Ni_{81}Fe_{19}/PtO_x/PtO_y/Pt$ device measured after removing the applied voltages of ± 35 V is plotted correspondingly. (**D**) Schematic of the experimental setup for the application of the gate voltages used to drive O^{2-} migration. O^{2-} migrates toward the $Ni_{81}Fe_{19}/Pt(O)$ interface for the application of the positive gate voltage (left), whereas the negative gate voltage drives O^{2-} away from the $Ni_{81}Fe_{19}/Pt(O)$ interface (right). (**E**) Typical current-voltage (I-V) curves measured across the $Ni_{81}Fe_{19}/PtO_x/PtO_y/Pt$ junction. The offset of the curves in the vertical direction was shifted for comparison.

Downloaded from http://advances.sciencemag.org/ on September 22, 2019

due to the high oxygen incorporation in the PtO_x layer. In contrast, the application of the negative gate voltage (0 V → −35 V → 0 V), which drives O^{2-} away from the $Ni_{81}Fe_{19}$/Pt(O) interface, results in a decrease of the *S*/*A* ratio. This is consistent with the oxidation level dependence of the ST-FMR spectral shape shown in Fig. 2C, where the *S*/*A* ratio increases by increasing the oxidation level in the $Ni_{81}Fe_{19}$/Pt(O) bilayer.

The reversible switching of the ST-FMR spectral shape was observed only when the large voltages (± 35 V) were applied. This result indicates a nonvolatile characteristic when large gate voltages (± 35 V) are applied, whereas relative low gate voltages result in a volatile characteristic. These differences also appear in the current-voltage (*I*-*V*) curves shown in Fig. 6E. When gate voltages of up to 30 V are applied, the curve follows an almost identical history, which corresponds to a volatile O^{2-} migration. On the other hand, by applying voltages of up to 35 V, a resistive switching characteristic is observed in the *I*-*V* curve, indicating a nonvolatile O^{2-} migration.

During the reversible switching of the spin-orbit torque generation, although a possible O^{2-} migration into the $Ni_{81}Fe_{19}$ layer can also change the *S*/*A* ratio, the oxidation of the $Ni_{81}Fe_{19}$ layer cannot be responsible for the change of the ST-FMR spectra. Because the gate voltage is applied along the perpendicular direction of the device (Fig. 6D), if the O^{2-} migrates into the $Ni_{81}Fe_{19}$ layer, the electrical resistance along the in-plane direction of the $Ni_{81}Fe_{19}$ layer should change. However, as shown in Fig. 6C, we observed no change in the in-plane electrical resistance of the $Ni_{81}Fe_{19}$ layer in the $Ni_{81}Fe_{19}$/Pt(O)/Pt device after the application of ± 35 V. This result indicates that the oxidation of the $Ni_{81}Fe_{19}$ layer is negligible. A possible O^{2-} migration into the bottom nonoxidized Pt layer also plays a minor role in the voltage-induced change of the ST-FMR spectra. Although the spin-orbit torques generated by the spin Hall effect in the bottom Pt layer can be neglected because of the presence of the insulating Pt(O) layer in the $Ni_{81}Fe_{19}$/Pt(O)/Pt device, an Oersted field created by the rf charge current flowing in the bottom Pt layer may contribute to the ST-FMR signal. However, by applying a negative voltage, if the O^{2-} migrates into the bottom Pt layer, the effective thickness of the nonoxidized Pt layer should be decreased and thus the Oersted field should also be decreased. This is contrary to the fact that the *S*/*A* switching shown in Fig. 6C can be reproduced only when the negative (positive) voltage increases (decreases) the Oersted field. Therefore, the voltage-induced change of the ST-FMR spectral shape can be attributed to the O^{2-} migration within the highly resistive PtO_x/PtO_y bilayer; the O^{2-} migration in the PtO_x/PtO_y bilayer changes the oxidation level at the $Ni_{81}Fe_{19}$/PtO_x interface, which enables the tuning of the spin-orbit torque generation.

DISCUSSION

We have demonstrated current-induced magnetization switching using an electrically insulating spin-torque generator. By turning Pt into an electrical insulator through oxygen incorporation, we show that a robust damping-like torque can be generated purely through the interface SOC. The interface spin-orbit torque allows one to control the magnetization in a perpendicularly magnetized ferrimagnet sandwiched between insulating oxides. Currently, the underlying physics of the current-induced SOC effects is debatable because the spin-orbit torques originating from the bulk and interface SOC are difficult to disentangle in the metallic heterostructures. The electrically insulating spin-torque generator provides a model system to study the spin-orbit effects purely arising from the interface SOC.

In the MgO/CoTb/Pt(O) device used in the present study, a large current is necessary to switch the perpendicular magnetization. The reason for this is that most of the applied charge current flows in the bulk of the thick CoTb layer despite the fact that the spin-orbit torque responsible for the magnetization switching is purely generated by the interface current. Thus, the switching current can be decreased significantly by fabricating a thinner, perpendicularly magnetized film; the insulating spin-torque generator promises a way to minimize the switching energy of spin-based magnetic memories because of the absence of the energy dissipation in the bulk of the spin-torque generator. We also show that the spin-orbit effect can be tuned electrically by changing the oxidation level near the FM/Pt(O) interface through the voltage-driven O^{2-} migration in the oxygen-incorporated Pt layer. This finding is different from the previous report that the voltage-driven O^{2-} migration was used to oxidize an FM layer to tune the magnetic properties (*38*), because we use the voltage-driven O^{2-} migration to directly tune the spin-torque generator instead of the FM layer. Because the energy dissipation in the bulk can be avoided, our findings pave a way toward energy-efficient, voltage-programmable spintronic applications.

MATERIALS AND METHODS

The films were deposited on thermally oxidized Si substrates (SiO_2) by rf magnetron sputtering at room temperature. Before the deposition, the base pressure in the chamber was lower than 1×10^{-6} Pa and the deposition pressure was 0.2 Pa. The CoTb, $Ni_{81}Fe_{19}$, and SiO_2 films were deposited by applying argon gas with a flow of 10 standard cubic centimeters per minute. For the Pt(O) deposition, argon and oxygen gases were introduced into the chamber, and the amount of oxygen gas in the reactive mixture, *Q*, was altered to change the oxygen concentration in the Pt(O) films. The film thicknesses were controlled by the deposition time with a precalibrated deposition rate. For the fabrication of the devices used in the magnetization switching experiment, the substrates were patterned into a 20 μm × 80 μm Hall bar shape by standard photolithography before the deposition, and the lift-off technique was used to remove the rest part of the films after the deposition. For the fabrication of the devices used in the ST-FMR experiment, the substrates were patterned into a 10 μm × 150 μm rectangular shape. For the fabrication of the devices used in the experiment of the voltage tuning of the oxidation level at the $Ni_{81}Fe_{19}$/Pt(O) interface, a Pt film was oxidized by irradiation with accelerated oxygen particles passing through a 30 W biased electrode with cylindrical holes. The source power for inductively coupled oxygen plasma generation was an rf of 500 W. To investigate the microstructure of Pt(O), x-ray diffraction and x-ray reflectivity measurements were conducted with a Bruker D8 Discover diffractometer by applying CuK_α radiation. Single Pt(O) blanket films were fabricated by changing the oxygen flow for the measurements. The electrical resistivity of the Pt(O) and $Ni_{81}Fe_{19}$ films was measured using the conventional four-probe method. All measurements were conducted at room temperature.

SUPPLEMENTARY MATERIALS

Supplementary material for this article is available at http://advances.sciencemag.org/cgi/content/full/4/2/eaar2250/DC1

section S1. Materials' characterization
section S2. Second harmonic measurement of the AHE resistance
section S3. Current-induced magnetization switching
section S4. Damping modulation
section S5. Voltage control of spin-orbit torques
fig. S1. Characterization of Pt(O) films.
fig. S2. Second harmonic measurement of the AHE resistance.
fig. S3. Planar Hall effect resistance.

Downloaded from http://advances.sciencemag.org/ on September 22, 2019

fig. S4. Pt(O) layer thickness dependence of the second harmonic AHE resistance.
fig. S5. Current-induced magnetization switching.
fig. S6. Damping modulation.
fig. S7. Device fabrication process.
fig. S8. Voltage control of spin-orbit torques.

REFERENCES AND NOTES

1. J. Sinova, S. O. Valenzuela, J. Wunderlich, C. H. Back, T. Jungwirth, Spin Hall effects. *Rev. Mod. Phys.* **87**, 1213–1260 (2015).
2. T. Jungwirth, J. Wunderlich, K. Olejnik, Spin Hall effect devices. *Nat. Mater.* **11**, 382–390 (2012).
3. A. Manchon, H. C. Koo, J. Nitta, S. M. Frolov, R. A. Duine, New perspectives for Rashba spin–orbit coupling. *Nat. Mater.* **14**, 871–882 (2015).
4. A. Soumyanarayanan, N. Reyren, A. Fert, C. Panagopoulos, Emergent phenomena induced by spin–orbit coupling at surfaces and interfaces. *Nature* **539**, 509–517 (2016).
5. I. M. Miron, K. Garello, G. Gaudin, P.-J. Zermatten, M. V. Costache, S. Auffret, S. Bandiera, B. Rodmacq, A. Schuhl, P. Gambardella, Perpendicular switching of a single ferromagnetic layer induced by in-plane current injection. *Nature* **476**, 189–193 (2011).
6. I. M. Miron, G. Gaudin, S. Auffret, B. Rodmacq, A. Schuhl, S. Pizzini, J. Vogel, P. Gambardella, Current-driven spin torque induced by the Rashba effect in a ferromagnetic metal layer. *Nat. Mater.* **9**, 230–234 (2010).
7. L. Liu, C.-F. Pai, Y. Li, H. W. Tseng, D. C. Ralph, R. A. Buhrman, Spin-torque switching with the giant spin Hall effect of tantalum. *Science* **336**, 555–558 (2012).
8. J. Kim, J. Sinha, M. Hayashi, M. Yamanouchi, S. Fukami, T. Suzuki, S. Mitani, H. Ohno, Layer thickness dependence of the current-induced effective field vector in Ta|CoFeB|MgO. *Nat. Mater.* **12**, 240–245 (2013).
9. G. Yu, P. Upadhyaya, Y. Fan, J. G. Alzate, W. Jiang, K. L. Wong, S. Takei, S. A. Bender, L.-T. Chang, Y. Jiang, M. Lang, J. Tang, Y. Wang, Y. Tserkovnyak, P. K. Amiri, K. L. Wang, Switching of perpendicular magnetization by spin–orbit torques in the absence of external magnetic fields. *Nat. Nanotechnol.* **9**, 548–554 (2014).
10. Y. Fan, P. Upadhyaya, X. Kou, M. Lang, S. Takei, Z. Wang, J. Tang, L. He, L.-T. Chang, M. Montazeri, G. Yu, W. Jiang, T. Nie, R. N. Schwartz, Y. Tserkovnyak, K. L. Wang, Magnetization switching through giant spin–orbit torque in a magnetically doped topological insulator heterostructure. *Nat. Mater.* **13**, 699–704 (2014).
11. X. Wang, C. O. Pauyac, A. Manchon, Spin-orbit-coupled transport and spin torque in a ferromagnetic heterostructure. *Phys. Rev. B* **89**, 054405 (2014).
12. K. Garello, I. M. Miron, C. O. Avci, F. Freimuth, Y. Mokrousov, S. Blügel, S. Auffret, O. Boulle, G. Gaudin, P. Gambardella, Symmetry and magnitude of spin–orbit torques in ferromagnetic heterostructures. *Nat. Nanotechnol.* **8**, 587–593 (2013).
13. X. Fan, J. Wu, Y. Chen, M. J. Jerry, H. Zhang, J. Q. Xiao, Observation of the nonlocal spin-orbital effective field. *Nat. Commun.* **4**, 1799 (2013).
14. Y. Fan, X. Kou, P. Upadhyaya, Q. Shao, L. Pan, M. Lang, X. Che, J. Tang, M. Montazeri, K. Murata, L.-T. Chang, M. Akyol, G. Yu, T. Nie, K. L. Wong, J. Liu, Y. Wang, Y. Tserkovnyak, K. L. Wang, Electric-field control of spin–orbit torque in a magnetically doped topological insulator. *Nat. Nanotechnol.* **11**, 352–359 (2016).
15. K.-U. Demasius, T. Phung, W. Zhang, B. P. Hughes, S.-H. Yang, A. Kellock, W. Han, A. Pushp, S. S. P. Parkin, Enhanced spin–orbit torques by oxygen incorporation in tungsten films. *Nat. Commun.* **7**, 10644 (2016).
16. P. M. Haney, H.-W. Lee, K.-J. Lee, A. Manchon, M. D. Stiles, Current induced torques and interfacial spin-orbit coupling: Semiclassical modeling. *Phys. Rev. B* **87**, 174411 (2013).
17. D. A. Pesin, A. H. MacDonald, Quantum kinetic theory of current-induced torques in Rashba ferromagnets. *Phys. Rev. B* **86**, 014416 (2012).
18. J. Finley, L. Liu, Spin-orbit-torque efficiency in compensated ferrimagnetic cobalt-terbium alloys. *Phys. Rev. Appl.* **6**, 054001 (2016).
19. J. Han, A. Richardella, S. A. Siddiqui, J. Finley, N. Samarth, L. Liu, Room-temperature spin-orbit torque switching induced by a topological insulator. *Phys. Rev. Lett.* **119**, 077702 (2017).
20. Y. Abe, M. Kawamura, K. Sasaki, Effects of oxygen gettering and target mode change in the formation process of reactively sputtered Pt oxide thin films. *J. Vac. Sci. Technol. A* **18**, 2608–2612 (2000).
21. M. T. Johnson, J. J. de Vries, N. W. E. McGee, J. aan de Stegge, F. J. A. den Broeder, Orientational dependence of the interface magnetic anisotropy in epitaxial Ni/Co/Ni sandwiches. *Phys. Rev. Lett.* **69**, 3575–3578 (1992).
22. P. Hansen, C. Clausen, G. Much, M. Rosenkranz, K. Witter, Magnetic and magneto-optical properties of rare-earth transition-metal alloys containing Gd, Tb, Fe, Co. *J. Appl. Phys.* **66**, 756–767 (1989).
23. M. Akyol, J. G. Alzate, G. Yu, P. Upadhyaya, K. L. Wong, A. Ekicibil, P. K. Amiri, K. L. Wang, Effect of the oxide layer on current-induced spin-orbit torques in Hf|CoFeB|MgO and Hf|CoFeB|TaO_x structures. *Appl. Phys. Lett.* **106**, 032406 (2015).
24. Y. Ou, C.-F. Pai, S. Shi, D. C. Ralph, R. A. Buhrman, Origin of fieldlike spin-orbit torques in heavy metal/ferromagnet/oxide thin film heterostructures. *Phys. Rev. B* **94**, 140414 (2016).
25. L. Liu, T. Moriyama, D. C. Ralph, R. A. Buhrman, Spin-torque ferromagnetic resonance induced by the spin Hall effect. *Phys. Rev. Lett.* **106**, 036601 (2011).
26. W. Zhang, W. Han, X. Jiang, S.-H. Yang, S. S. P. Parkin, Role of transparency of platinum–ferromagnet interfaces in determining the intrinsic magnitude of the spin Hall effect. *Nat. Phys.* **11**, 496–502 (2015).
27. C.-F. Pai, Y. Ou, L. H. Vilela-Leão, D. C. Ralph, R. A. Buhrman, Dependence of the efficiency of spin Hall torque on the transparency of Pt/ferromagnetic layer interfaces. *Phys. Rev. B* **92**, 064426 (2015).
28. K. Kondou, H. Sukegawa, S. Kasai, S. Mitani, Y. Niimi, Y. Otani, Influence of inverse spin Hall effect in spin-torque ferromagnetic resonance measurements. *Appl. Phys. Express* **9**, 023002 (2016).
29. Y. Tserkovnyak, A. Brataas, G. E. W. Bauer, Enhanced Gilbert damping in thin ferromagnetic films. *Phys. Rev. Lett.* **88**, 117601 (2002).
30. Y. Niimi, Y. Otani, Reciprocal spin Hall effects in conductors with strong spin–orbit coupling: A review. *Rep. Prog. Phys.* **78**, 124501 (2015).
31. L. Wang, R. J. H. Wesselink, Y. Liu, Z. Yuan, K. Xia, P. J. Kelly, Giant room temperature interface spin Hall and inverse spin Hall effects. *Phys. Rev. Lett.* **116**, 196602 (2016).
32. V. P. Amin, M. D. Stiles, Spin transport at interfaces with spin-orbit coupling: Phenomenology. *Phys. Rev. B* **94**, 104420 (2016).
33. H. Kurebayashi, J. Sinova, D. Fang, A. C. Irvine, T. D. Skinner, J. Wunderlich, V. Novák, R. P. Campion, B. L. Gallagher, E. K. Vehstedt, L. P. Zârbo, K. Výborný, A. J. Ferguson, T. Jungwirth, An antidamping spin–orbit torque originating from the Berry curvature. *Nat. Nanotechnol.* **9**, 211–217 (2014).
34. J. C. R. Sánchez, L. Vila, G. Desfonds, S. Gambarelli, J. P. Attané, J. M. De Teresa, C. Magén, A. Fert, Spin-to-charge conversion using Rashba coupling at the interface between non-magnetic materials. *Nat. Commun.* **4**, 2944 (2013).
35. K. Kondou, R. Yoshimi, A. Tsukazaki, Y. Fukuma, J. Matsuno, K. S. Takahashi, M. Kawasaki, Y. Tokura, Y. Otani, Fermi-level-dependent charge-to-spin current conversion by Dirac surface states of topological insulators. *Nat. Phys.* **12**, 1027–1031 (2016).
36. R. Waser, R. Dittmann, G. Staikov, K. Szot, Redox-based resistive switching memories—Nanoionic mechanisms, prospects, and challenges. *Adv. Mater.* **21**, 2632–2663 (2009).
37. J. J. Yang, D. B. Strukov, D. R. Stewart, Memristive devices for computing. *Nat. Nanotechnol.* **8**, 13–24 (2013).
38. U. Bauer, L. Yao, A. J. Tan, P. Agrawal, S. Emori, H. L. Tuller, S. van Dijken, G. S. D. Beach, Magneto-ionic control of interfacial magnetism. *Nat. Mater.* **14**, 174–181 (2015).
39. J. J. Yang, M. D. Pickett, X. Li, D. A. A. Ohlberg, D. R. Stewart, R. S. Williams, Memristive switching mechanism for metal/oxide/metal nanodevices. *Nat. Nanotechnol.* **3**, 429–433 (2008).
40. J. J. Yang, J. Borghetti, D. Murphy, D. R. Stewart, R. S. Williams, A family of electronically reconfigurable nanodevices. *Adv. Mater.* **21**, 3754–3758 (2009).
41. M.-J. Lee, C. B. Lee, D. Lee, S. R. Lee, M. Chang, J. H. Hur, Y.-B. Kim, C.-J. Kim, D. H. Seo, S. Seo, U.-I. Chung, I.-K. Yoo, K. Kim, A fast, high-endurance and scalable non-volatile memory device made from asymmetric Ta_2O_{5-x}/TaO_{2-x} bilayer structures. *Nat. Mater.* **10**, 625–630 (2011).
42. J. S. Lee, S. Lee, T. W. Noh, Resistive switching phenomena: A review of statistical physics approaches. *Appl. Phys. Rev.* **2**, 031303 (2015).
43. S. Panda, D. J. Economou, L. Chen, Anisotropic etching of polymer films by high energy (~100s of eV) oxygen atom neutral beams. *J. Vac. Sci. Technol. A* **19**, 398–404 (2001).
44. T. Ohno, S. Samukawa, Resistive switching in a few nanometers thick tantalum oxide film formed by a metal oxidation. *Appl. Phys. Lett.* **106**, 173110 (2015).

Acknowledgments

Funding: This work was supported by Japan Society for the Promotion of Science (JSPS) KAKENHI grant nos. 26220604 and 26103004; PRESTO-JST "Innovative nano-electronics through interdisciplinary collaboration among material, device and system layers" grant nos. 13415036, JPMJPR1323, and JPMJPR1325; the Mizuho Foundation for the Promotion of Sciences; JSPS Core-to-Core Program; and Spintronics Research Network of Japan (Spin-RNJ). H.A. acknowledges the support from the JSPS Fellowship (nos. P17066 and 17F17066). T.O. thanks S. Samukawa for fruitful discussion on the plasma technique. **Author contributions:** H.A. and T.O. fabricated the devices and collected the data. H.A., T.O., Y. Kanno, Y. Kageyama, and Y.M. analyzed the data. K.A., T.O., H.M., and J.S. designed the experiments and developed the explanation. K.A., T.O., and H.A. wrote the manuscript. All authors discussed the results and reviewed the manuscript. H.A. was responsible for all the figures in the main text and the Supplementary Materials. **Competing interests:** The authors declare that they have no competing interests. **Data and materials availability:** All data needed to evaluate the conclusions in the paper are present in the paper and/or the Supplementary Materials. Additional data related to this paper may be requested from the authors.

Submitted 16 October 2017
Accepted 19 January 2018
Published 23 February 2018
10.1126/sciadv.aar2250

Citation: H. An, T. Ohno, Y. Kanno, Y. Kageyama, Y. Monnai, H. Maki, J. Shi, K. Ando, Current-induced magnetization switching using an electrically insulating spin-torque generator. *Sci. Adv.* **4**, eaar2250 (2018).

Downloaded from http://advances.sciencemag.org/ on September 22, 2019

Science Advances

Current-induced magnetization switching using an electrically insulating spin-torque generator

Hongyu An, Takeo Ohno, Yusuke Kanno, Yuito Kageyama, Yasuaki Monnai, Hideyuki Maki, Ji Shi and Kazuya Ando

Sci Adv **4** (2), eaar2250.
DOI: 10.1126/sciadv.aar2250

ARTICLE TOOLS http://advances.sciencemag.org/content/4/2/eaar2250

SUPPLEMENTARY MATERIALS http://advances.sciencemag.org/content/suppl/2018/02/16/4.2.eaar2250.DC1

REFERENCES This article cites 44 articles, 1 of which you can access for free
http://advances.sciencemag.org/content/4/2/eaar2250#BIBL

PERMISSIONS http://www.sciencemag.org/help/reprints-and-permissions

Use of this article is subject to the Terms of Service

Science Advances (ISSN 2375-2548) is published by the American Association for the Advancement of Science, 1200 New York Avenue NW, Washington, DC 20005. 2017 © The Authors, some rights reserved; exclusive licensee American Association for the Advancement of Science. No claim to original U.S. Government Works. The title *Science Advances* is a registered trademark of AAAS.

Downloaded from http://advances.sciencemag.org/ on September 22, 2019